UC Office of the President
Recent Work

Title
Magnesium oxide at extreme temperatures and pressures studied with first-principles simulations

Permalink
https://escholarship.org/uc/item/1pv7x5x9

Journal
The Journal of Chemical Physics, 151(21)

ISSN
0021-9606 1089-7690

Authors
Soubiran, François
González-Cataldo, Felipe
Driver, Kevin P
et al.

Publication Date
2019-12-07

DOI
10.1063/1.5126624

Peer reviewed

Magnesium oxide at extreme temperatures and pressures studied with first-principles simulations

François Soubiran (iD), Felipe González-Cataldo (iD), Kevin P. Driver (iD), Shuai Zhang (iD), and Burkhard Militzer (iD)

View Online   Export Citation   CrossMark

ARTICLES YOU MAY BE INTERESTED IN

Magnesium oxide at extreme temperatures and pressures studied with first-principles simulations

François Soubiran,[1,2,a] (iD) Felipe González-Cataldo,[1] (iD) Kevin P. Driver,[1,3] (iD) Shuai Zhang,[1,4] (iD)
and Burkhard Militzer[1,5,b] (iD)

AFFILIATIONS

[1] Department of Earth and Planetary Science, University of California, Berkeley, California 94720, USA
[2] École Normale Supérieure de Lyon, Université Lyon 1, Laboratoire de Géologie de Lyon, CNRS UMR 5276, 69364 Lyon Cedex 07, France
[3] Lawrence Livermore National Laboratory, Livermore, California 94550, USA
[4] Laboratory for Laser Energetics, University of Rochester, Rochester, New York 14623, USA
[5] Department of Astronomy, University of California, Berkeley, California 94720, USA

[a] francois.soubiran@ens-lyon.org
[b] militzer@berkeley.edu

ABSTRACT

We combine two first-principles computer simulation techniques, path integral Monte Carlo and density functional theory molecular dynamics, to determine the equation of state of magnesium oxide in the regime of warm dense matter, with densities ranging from 0.35 to 71 g cm^{-3} and temperatures ranging from 10 000 K to 5×10^8 K. These conditions are relevant for the interiors of giant planets and stars as well as for shock wave compression measurements and inertial confinement fusion experiments. We study the electronic structure of MgO and the ionization mechanisms as a function of density and temperature. We show that the L-shell orbitals of magnesium and oxygen hybridize at high density. This results in a gradual ionization of the L-shell with increasing density and temperature. In this regard, MgO behaves differently from pure oxygen, which is reflected in the shape of the MgO principal shock Hugoniot curve. The curve of oxygen shows two compression maxima, while that of MgO shows only one. We predict a maximum compression ratio of 4.66 to occur for a temperature of 6.73×10^7 K. Finally, we study how multiple shocks and ramp waves can be used to cover a large range of densities and temperatures.

Published under license by AIP Publishing. https://doi.org/10.1063/1.5126624

I. INTRODUCTION

The discovery of numerous exoplanets[1] has renewed the interest in materials at extreme conditions since their behavior determines a planet's internal structure and evolution. Laboratory experiments and computer simulations have both contributed significantly to the characterization of matter at extreme conditions. Developing accurate equations of state (EOSs) for candidate materials is necessary not only to infer planetary formation scenarios but also to understand how materials respond to extreme conditions including those present in high-velocity impacts, shock compression, and inertial confinement fusion (ICF) experiments.[2] These applications require an EOS that is able to describe different degrees of ionization as the temperatures can increase by several orders of magnitude during these dynamic compression events. Inconsistencies in the EOS can lead to incorrect interpretations of the experiments or to contradicting planet formation scenarios that arise, for example, from different relations between isentropes and melting curves.[3]

Magnesium oxide (MgO) is one of the most abundant minerals in the Earth's interior and is considered to be a primary

building block of planetary formation.[4,5] It is commonly used as a representative mantle material in exoplanet modeling.[4,6–8] Shock compression experiments on SiO_2[9,10] and MgO,[5,11,12] combined with first principle calculations, demonstrated that these mantle minerals become electrically conducting in the fluid phase. Super-Earth planets can thus generate magnetic fields within their mantles.[13] At ambient conditions, MgO has the rock-salt (B1) structure that is known from experiments to be stable up to at least 227 GPa.[14] Around 500 GPa, it is predicted to transform into the CsCl (B2) structure,[15–17] which is believed to be the only stable phase up to at least 40 Mbar, a pressure at which MgO remains solid at least up to 20 000 K.[18] Together with silica (SiO_2), MgO is one of the endmembers on the last-stage dissociation of $MgSiO_3$.[16,19–21]

Recent experiments using plate impacts have measured the shock Hugoniot of a single-crystal MgO preheated to 1850 K, reaching temperatures up to 9100 K and providing a complete EOS for pressures below 250 GPa.[22] The principal Hugoniot of MgO has been explored in the solid and liquid phases using plate impacts up to 1200 GPa.[23] More extreme conditions have been achieved with laser-driven shocks,[24] providing measurements of the reflectivity, specific heat, and Grüneisen parameter up to 2300 GPa and 64 000 K. According to these experiments, the commonly used tabulated EOSs, such as SESAME[85] and LEOS,[86] have underpredicted the temperature for a given pressure in liquid MgO. Although the melting curve of MgO has been explored with first-principles simulations up to 4000 GPa,[25] the properties of the liquid have not been studied for temperatures higher than a few thousand K,[26,27] where significant ionization can take place and an accurate description is required in order to interpret the latest high-temperature experiments on MgO. Recently, the properties of the $MgSiO_3$ plasma have been reported in the warm-dense matter regime,[28] where it was shown that the K-shell ionization of the oxygen atoms is the cause of a compression maximum along the principal Hugoniot of $MgSiO_3$. This provides an insight into the properties of silicates in the warm-dense matter regime, but a full picture is far from complete. Therefore, a consistent EOS that spans a wide range of temperatures and pressures is needed in order to provide a quantitative picture that accounts for the changes in MgO properties with pressure and temperature.

Path integral Monte Carlo (PIMC) methods have gained considerable interest as a state-of-the-art, stochastic first-principles technique for computing the properties of interacting quantum systems at finite temperature. This formalism results in a highly parallelizable implementation and an accurate description of the properties of materials at high temperature where the electrons are excited to a significant degree.[29–33] The application of the PIMC method to first and second-row elements has been possible due to the development of free-particle[34,35] and Hartree-Fock nodes.[36] The latter approach enables one to efficiently incorporate localized electronic states into the nodal structure, which extends the applicability of the path integral formalism to heavier elements and lower temperatures.[37,38] Furthermore, PIMC treats all electrons explicitly, avoiding the use of any pseudopotentials. The PIMC simulation time scales as $1/T$, proportional to the length of the paths, which is efficient at high-temperature conditions, where most electrons including the K shell are excited. The accuracy of PIMC at intermediate temperatures has been shown[39,40] to be in good agreement

with predictions from density functional theory molecular dynamics (DFT-MD) simulations.

Kohn-Sham (KS) DFT[41,42] is a first-principles simulation method that determines the ground state of quantum systems with high efficiency and reasonable accuracy, which has made it a workhorse of computational materials science. It has thus gained considerable use for many years. The introduction of the Mermin scheme[43] enabled the inclusion of excited electronic states, which extended the applicability range of the DFT method to higher temperatures. The combination of this method with molecular dynamics has been widely applied to compute the EOS of condensed matter, warm dense matter (WDM), and dense plasmas.[44–47] It is often the most suitable computation method to derive the EOS under a wide range of conditions because it accounts for both electronic shell and bonding effects. The main source of uncertainty in DFT is the use of an approximate exchange-correlation (XC) functional. The error in the XC functional is generally a negligible fraction of the internal energy, which is the most relevant quantity for the EOS and the derivation of the shock Hugoniot curve.[48] However, the range of validity of this assumption in the WDM regime remains to be verified for different classes of materials through the comparison with laboratory experiments and other simulation methods such as PIMC.

In this work, we combine the PIMC and DFT-MD methods to study the properties of MgO in the regime of WDM. The combination of both methods allows us to test the validity of the approximations in the methods. We study the regimes of thermal and pressure ionization of the electronic shells and provide an equation of state that spans a wide range of temperatures and pressure. We describe the electronic properties of liquid MgO and show how the bandgap between s and p states closes upon compression and provide a structural characterization of the liquid. Finally, we compare our PIMC/DFT-MD shock Hugoniot curves with widely used models and experiments.

II. SIMULATIONS METHODS

We perform first-principles computer simulations of magnesium oxide for a range of extreme density and temperature conditions that we illustrate in Fig. 1. At high temperatures, we employ path integral Monte Carlo (PIMC) simulations, and at lower temperatures, we use standard Kohn-Sham density functional theory molecular dynamics (DFT-MD) calculations.

A. PIMC

PIMC is a state-of-the-art first-principles technique for simulating interacting quantum systems at finite temperatures. The fundamental techniques for the simulations of bosonic systems were developed in Ref. 49 and later reviewed in Ref. 34. Subsequently, the algorithm was extended to simulate fermionic systems by introducing the *restricted* paths approach.[35,50,51] The first results of this simulation method were reported in the seminal work on liquid ^3He[51] and dense hydrogen.[52] In subsequent articles, this method was applied to study hydrogen,[53–58] helium,[29,39,59] hydrogen-helium mixtures,[60] and one-component plasmas.[61–63] In recent years, the PIMC method was extended to simulate plasmas of various
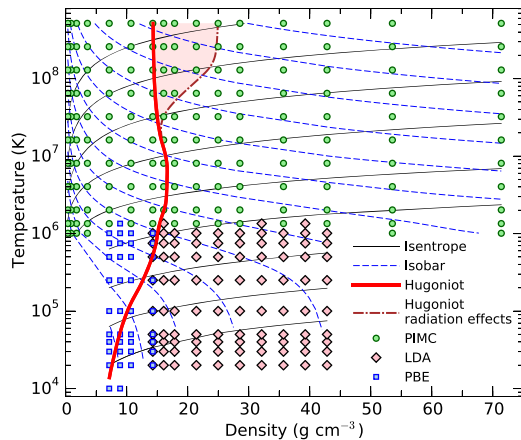
FIG. 1. Temperature-density conditions of our PIMC and DFT-MD simulations along with computed isobars, isentropes, and shock Hugoniot curves that were with and without radiation effects for an initial density of ρ_0 = 3.570 g cm^{-3} (V_0 = 18.747 821 6 Å/f.u.).

first-row elements[30,40,47,64–66] and with the development of Hartree-Fock nodes, the simulations of second-row elements became possible.[32,36–38]

This PIMC method is based on the thermal density matrix of a quantum system, $\hat{\rho} = e^{-\beta\hat{\mathcal{H}}}$, which is expressed as a product of higher-temperature matrices by means of the identity $e^{-\beta\hat{\mathcal{H}}} = (e^{-\tau\hat{\mathcal{H}}})^M$, where M is an integer and $\tau \equiv \beta/M$ represents the time step of a path integral in imaginary time. The path integral emerges when the operator $\hat{\rho}$ is evaluated in real space,

$$\langle \mathbf{R}|\hat{\rho}|\mathbf{R}'\rangle = \frac{1}{N!}\sum_{\mathcal{P}}(-1)^{\mathcal{P}}\oint_{\mathbf{R}\to\mathcal{P}\mathbf{R}'}\mathbf{dR}_t\,e^{-S[\mathbf{R}_t]}. \quad (1)$$

Here, we have already summed over all permutations, $\mathcal{P}$, of all N identical fermions in order to project out all antisymmetric states. For sufficiently small time steps, τ, all many-body correlation effects vanish and the action, $S[\mathbf{R}_t]$, can be computed by solving a series of two-particle problems.[49,67,68] The advantage of this approach is that all many-body quantum correlations are recovered through the integration over all paths. The integration also enables one to compute quantum mechanical expectation values of thermodynamic observables, such as the kinetic and potential energies, pressure, pair correlation functions, and momentum distribution.[34,69] Most practical implementations of the path integral techniques rely on Monte Carlo sampling techniques because the integral has $D \times N \times M$ dimensions (D is the dimension in space) and, in addition, one needs to sum over all permutations. The method becomes increasingly efficient at high temperature because the length of the paths scales like $1/T$. In the limit of low temperature, where few electronic excitations are present, the PIMC method becomes computationally demanding and the MC sampling can become inefficient. Still, the PIMC method avoids any exchange-correlation approximation and the calculation of single-particle eigenstates, which are embedded in all DFT calculations.

The only uncontrolled approximation within fermionic PIMC calculations is the use of the fixed-node approximation, which restricts the paths in order to avoid the well-known fermion sign problem.[35,50,51] Addressing this problem in PIMC is crucial as it causes large fluctuations in computed averages due to the cancellation of positive and negative permutations in Eq. (1). We solve the sign problem approximately by restricting the paths to stay within nodes of a trial density matrix that we obtain from a Slater determinant of single-particle density matrices,

$$\rho_T(\mathbf{R}, \mathbf{R}'; \beta) = \left\| \rho^{[1]}(r_i, r_j'; \beta) \right\|_{ij}, \quad (2)$$

that combined free and bound electronic states,[36,38]

$$\rho^{[1]}(r, r'; \beta) = \sum_k e^{-\beta E_k}\Psi_k(r)\Psi_k^*(r') \quad (3)$$

$$+ \sum_{I=1}^{N}\sum_{s=0}^{n} e^{-\beta E_s}\Psi_s(r - R_I)\Psi_s^*(r' - R_I). \quad (4)$$

The first sum includes all plane waves, Ψ_k, while the second represents n bound states Ψ_s with energy E_s that are localized around all atoms I. Predictions from various slightly differing forms of this approach have been compared in Ref. 37.

All PIMC simulations used periodic boundary conditions and treated 80 electrons, 4 Mg, and 4 O nuclei explicitly. We enforced the nodal constraint in small steps of imaginary time of τ = 1/8192 hartree^{-1}, while the pair density matrices[68] were evaluated in steps of 1/1024 hartree^{-1}. This results in using between 2560 and 5 time slices for the temperature range that is studied with PIMC simulations here. These choices converged the internal energy per atom to better than 1%. We have shown that the associated error is small for relevant systems at sufficiently high temperatures.[70]

B. DFT-MD

Kohn-Sham (KS) DFT-MD[41,42] is a well-established method to compute the properties of matter in the warm dense matter regime. We thus used the DFT-MD code Vienna *Ab Initio* Simulation Package (VASP)[71] to perform simulations up to 2×10^6 K to complement the PIMC calculations. We restricted our DFT-MD calculations to a range of 2- to 12-fold the ambient density of MgO. We placed from 4 to 32 MgO formula units in a cubic box with periodic boundary conditions. It has been shown in previous work that such a small cell is not detrimental to the accuracy of the EOS data under such high temperatures.[38,66,72] To keep the temperature constant, we used a Nosé thermostat.[73,74] The time step was adapted to the density and the temperature and ranged from 0.25 to 8.33 fs for a total duration of several hundred time steps to ensure a relevant estimation of the thermodynamic quantities.

Regarding the DFT calculations, we used the Mermin scheme[43] and employed projector augmented wave[75] (PAW) pseudopotentials. We were however limited to the existing pseudopotentials of VASP and opted for hard ones with a 1s^2 frozen core for both magnesium and oxygen. The PAW sphere radius was 1.75 bohr for Mg and 1.1 bohr for O. We used the generalized gradient approximation Perdew-Burke-Ernzerhof (PBE)[76] functional for the lowest densities

as it has shown to give good results for MgO.[13] At high densities, the pseudopotentials in PBE were unable to give proper results and we switched to the local density approximation (LDA). We have a very good agreement between both functionals at 4-fold compression (see Sec. III A). For very high temperatures, the Mermin approach requires the computation of the excited states even for low occupation numbers. That is why we computed up to 6000 bands even for the reduced cell size of 8 atoms when we reached temperatures above 10^6 K. This high number of bands ensured that we computed all the bands up to an energy level associated with an occupation of 10^{-5}. The systematic error due to this band cutoff is below 0.1%. The energy cutoff for the plane wave basis set also had to be increased at high temperatures up to 7000 eV. We sampled the Brillouin zone with the Γ point only, which was found to be sufficient for the convergence of the thermodynamic quantities under the conditions of interest.

For the calculation of the density of state (DOS), we used the KS eigenenergy on snapshots sampled every 500 time steps to compute an instantaneous DOS. To obtain a smooth curve, we replaced each eigenvalue by a Gaussian centered on the eigenenergy and with an rms width of 0.5 eV. Each instantaneous DOS was aligned on its Fermi energy so that we could average them. The average DOS was then reshifted by the average value of the Fermi energy. We also computed the projected DOS (pDOS). Each eigenstate was locally projected on spherical harmonics centered on each nucleus. We could then average the contributions to the DOS by species and by the harmonics level.

III. RESULTS AND DISCUSSION

A. Equation of state

The internal energies that were derived in the VASP DFT-MD simulations with LDA and PBE functionals were shifted, respectively, by $-273.602\,039\,8$ and $-274.900\,614\,6$ hartree per MgO formula unit in order to make them compatible with the all-electron energies that we obtained with the PIMC simulations.

In Fig. 2, we plot the relative excess pressure and energy with respect to an ideal gas of nuclei and Fermi gas of electrons. Regarding the DFT part solely, there is good agreement between LDA and PBE calculations at 4-fold compression ensuring a smooth transition from one data set to another. As temperature increases, DFT becomes too computationally expensive around the same conditions that PIMC first becomes viable. For MgO, we managed to obtain good agreement between PIMC and DFT at 1 347 305 K. Near this temperature, the relative difference in the pressure is less than 3.5%, and the difference in the energy ranges from 2.5 to 5.3 hartree/nucleus. These are maximum differences between PIMC and DFT-MD, as they are reported for the 12-fold compression case, where we are most severely affected by pseudopotential overlap and frozen core effects. Globally, the agreement is very satisfactory.

With our PIMC simulations, we were able to reach densities as low as 0.1 times the ambient density but not with DFT because of numerical limitations (both in computer time and in memory needs). For high densities, DFT was limited by the pseudopotentials available, preventing any simulations beyond 12-fold compression. However, as shown in Fig. 3, our data set still covers an
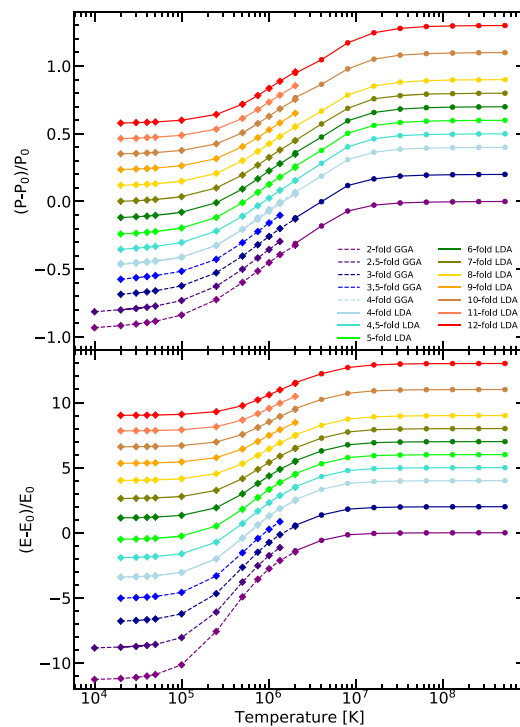

FIG. 2. Reduced equation of state of MgO from 2 to 12-fold compression from ambient density as a function of temperature as predicted by DFT (diamonds) and PIMC (circles). The top panel is the relative difference between the total pressure P and the pressure P_0 of an ideal gas of nuclei and a Fermi gas of electrons. The bottom panel is the difference between the total internal energy E and the energy E_0 of an ideal gas of nuclei and a Fermi gas of electrons. Different isochores have been shifted apart for clarity.
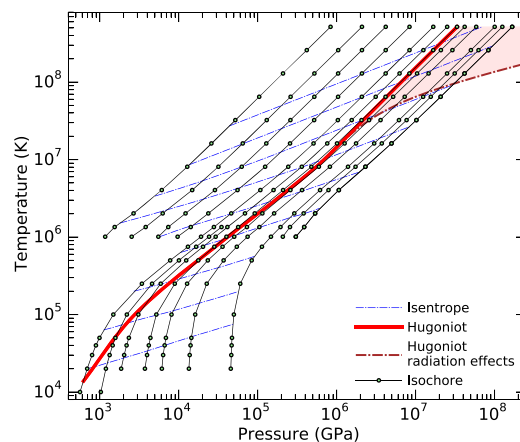

FIG. 3. Temperature-pressure conditions for the PIMC and DFT-MD calculations along isochores corresponding to the densities of 0.1-fold (upper left curve) to 20-fold (right curve) ambient density. The shock Hugoniot curves with and without radiation effects were included as well as a number of isentropes.

extremely wide range of pressures and temperatures. Our entire EOS table is provided as the supplementary material. This allows us to benchmark other faster but more approximate EOS methods for a wide range of conditions.

To extrapolate the present EOS toward other conditions, it is possible to use other approximations such as the fully ionized plasma[77] for high densities or a chemical model at low densities. Such an approach has been recently performed on H–He mixtures.[78] It is also possible to improve the EOS by a careful characterization of the free energy using thermodynamic integration. This work has been performed on H–He at temperatures relevant for the interior of giant planets.[79]

B. Electronic and ionic structures

From PIMC simulations, a measure of the degree of ionization can be obtained from the integrated nucleus-electron pair correlation function, $N(r)$, given by

$$N(r) = \left\langle \frac{1}{N_I} \sum_{e,I} \Theta\left(r - \|\vec{r}_e - \vec{r}_I\|\right) \right\rangle, \tag{5}$$

where $N(r)$ represents the average number of electrons within a sphere of radius r around a given nucleus of atom of type I. The summation includes all electron-nucleus pairs and Θ represents the Heaviside function. Figure 4 shows the integrated nucleus-electron
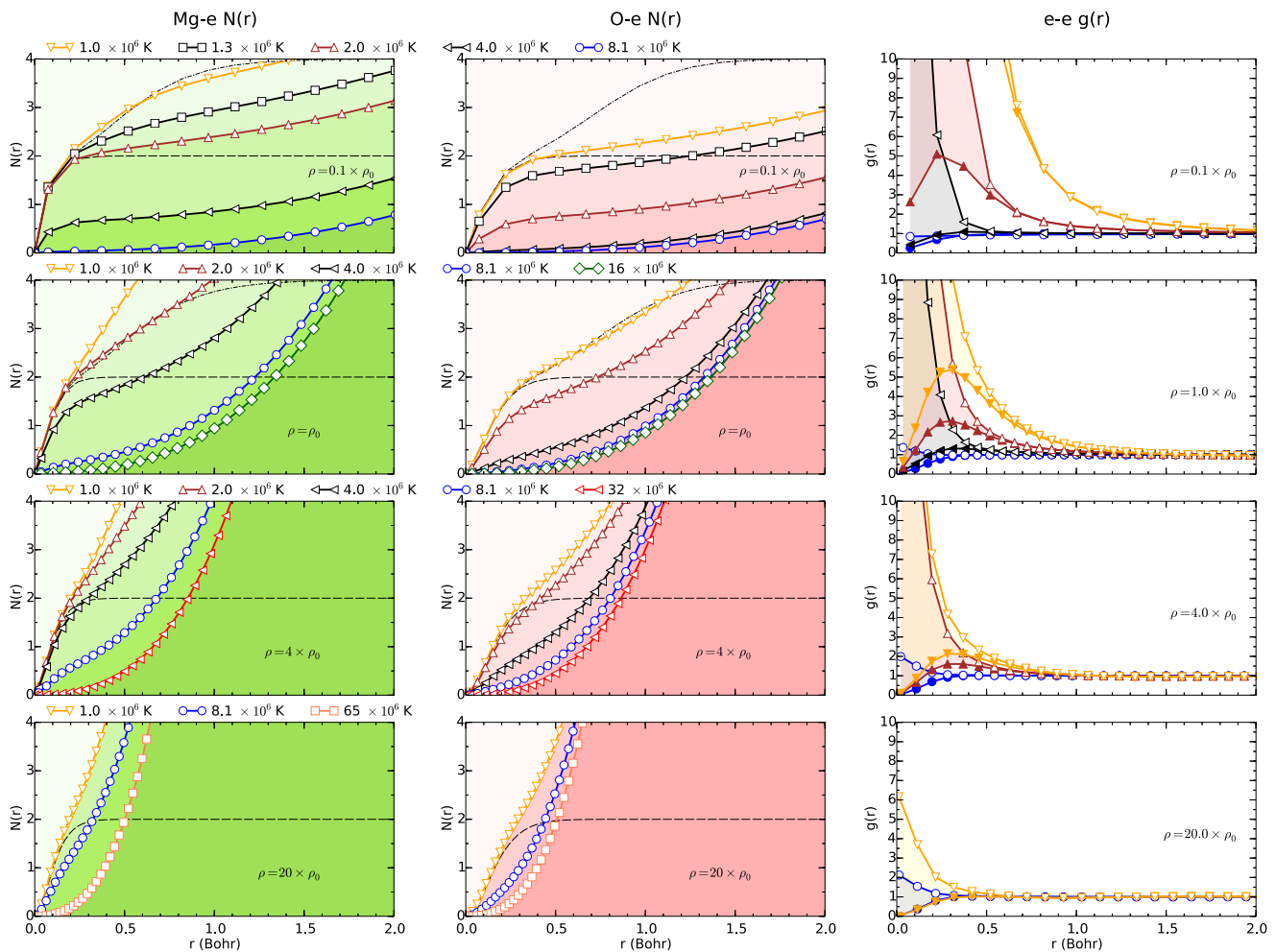

FIG. 4. The left and middle columns show the integrated nuclear-electron pair correlation function, $N(r)$, for Mg and O nuclei, respectively. In the right column, we plot the electron-electron correlation functions, $g(r)$, for a pair of electrons with parallel (filled symbols) and antiparallel spins (open symbols). All curves were derived from PIMC simulations. The four rows show results for different densities of ranging from 0.1, 1.0, 4.0, and 20.0 times the ambient density of 3.569 856 g cm^{-3}. The $N(r)$ functions represent the average of number of electrons contained within a sphere of radius, r, around a given nucleus. For comparison, we show the corresponding functions with thin dashed lines for isolated nuclei with double occupied 1s core states that we computed with the GAMESS software.[80] For the lowest two densities, the thin dotted-dashed lines show the curve for double occupied 1s and 2s states.

pair correlation function for temperatures from 1×10^6 K to 65×10^6 K and densities from 0.357 g cm^{-3} (0.1-fold) to 71.40 g cm^{-3} (20-fold compression). For comparison, the $N(r)$ functions of an isolated nucleus with a doubly occupied 1s orbital were included. Unless the 1s state is ionized, its contribution will dominate the $N(r)$ function at small radii of $r < 0.2$ bohr. For larger radii, contributions from other electronic shells and neighboring nuclei will enter. Still, this is the most direct approach available to compare the degree of 1s ionization of both nuclei.

At 0.1-fold compression, the comparison with the corresponding curves for the isolated nuclei shows that the ionization of the 1s states of the Mg nuclei occurs over the temperature interval from 2.0 to 8.1×10^6 K. Conversely, the ionization of 1s state of the oxygen nuclei occurs from 1.3 to 4.0×10^6 K, which reflects the difference in binding energy that scales with the square of the nuclear charge, Z. Consistent with this interpretation, one finds no evidence of an ionization of the 2s states of Mg nuclei at 1.0×10^6 K, while those of the oxygen nuclei are partially ionized, as the comparison with calculations of isolated nuclei in Fig. 4 shows.

When the density is increased from 0.1- to 1.0-fold compression (the second row of panels in Fig. 4), the degree of 1s ionization is reduced. For the Mg and O nuclei, the $N(r)$ functions at small r are closer to doubly occupied 1s state than they were before. This trend continues as we increase the density to 4.0 and 20-fold compression. The degree of 1s ionization is consistently reduced with increasing density when the results are compared for the same temperature. Most noticeable are the deviations for a temperature of 8.1×10^6 K. At 0.1-fold compression, the 1s states of both nuclei are essentially fully ionized while they still appear to be partially occupied for this temperature at 20-fold compression.

In Fig. 4, we also show the electron-electron pair correlation functions, $g(r)$, that we derived from our all-electron PIMC simulations. Without any Coulomb interactions, this function would equal 1 for all r for electron pairs with opposite spin. This is also true for pairs with the same spin for large distances, but for small r, this function must drop to zero because of Pauli exclusion. The trend for very small r can be seen in the right column of Fig. 4 where we plot the $g(r)$ functions for the fully interacting MgO system. For all other r values, these functions are substantially modified by the Coulomb interaction effects, as expected. At low density and low temperature, one finds strong positive correlations that reflect the fact that electrons with both types of spins occupy bound states at the same nuclei. With increasing temperature, the electrons become ionized and the positive correlation disappears. At small r, Pauli exclusion dominates which introduces differences into the pair correlation functions between electrons with parallel and opposite spin. For large r, these functions are always very similar.

For lower temperature conditions that we studied with DFT-MD simulations, one can derive information about the electronic properties by analyzing the Kohn-Sham eigenstates. In Fig. 5, we plot the density of states (DOS) at 10^5 K for three different densities. The full DOS shows that the system becomes increasingly pressure ionized with increasing density. Peaks in the DOS, that are narrow at low density, broaden and merge with the continuum of free states. In the KS-DFT framework, we can also approximately decompose the DOS into contributions from different nuclei and
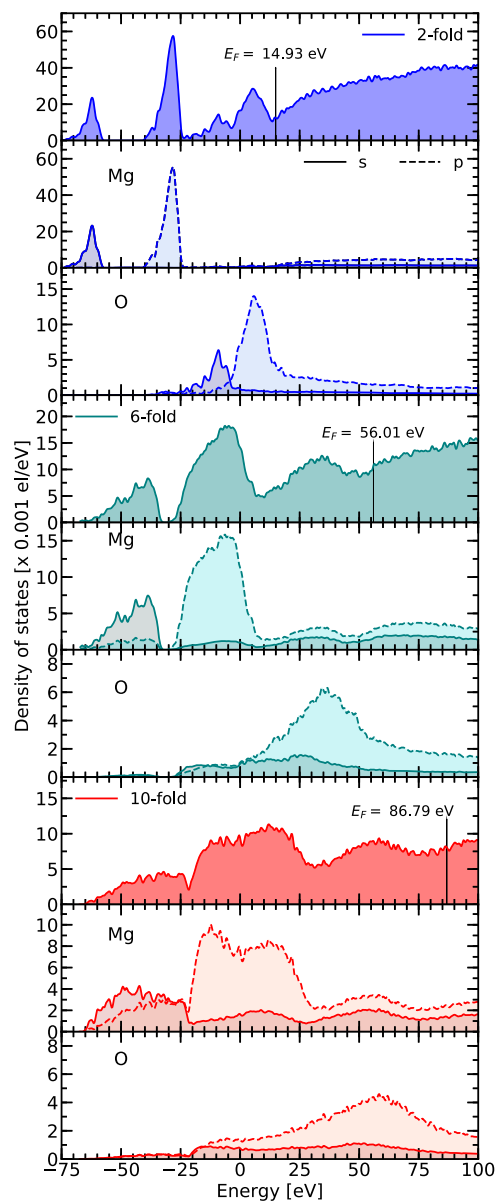

FIG. 5. Electronic density of states of MgO at 100 000 K. They are plotted for 2-fold (first three panels in blue), 6-fold (middle panels in green), and 10-fold (last three panels in red) compression. For each compression, we plotted the full DOS in the first panel, the projected DOS on s (solid) and p (dashed) orbitals of magnesium in the second panel, and the projected DOS on s and p orbitals of oxygen in the third panel. The DOS are aligned to the zero of energy of VASP. The vertical lines indicate the Fermi level.

orbital character. We included the results from various such projections in Fig. 5. At 2-fold compression, the first two peaks correspond to the L shell of magnesium while the M-shell states have already merged with the continuum. The second set of two peaks between −20 and 20 eV correspond to the s and p orbitals of oxygen L-shell. We retrieve a very similar feature in our simulations for pure

oxygen[72] that showed oxygen orbitals that could be distinguished clearly from the continuum.

As the density is increased, we can still identify two L-shell peaks of magnesium: a first one (L_I) with s character and a second ($L_{II,III}$) with p character. However, already at 6-fold and much more at 10-fold compression, both types of orbitals hybridize and form very broad peaks without a clear gap. For oxygen, the s-type peak has already disappeared at 6-fold which is very different from the predictions for pure oxygen.[81] However, it reminds one of the electronic properties of the carbon in dense plastics.[66] These phenomena are likely caused by the hybridization of the p orbital of magnesium with the s and p orbitals of oxygen. This produces a very large broadening of the oxygen L-band which gradually merges with the continuum with increasing density. The observed hybridization of magnesium and oxygen orbitals has thus consequences for the ionization state of MgO at extreme conditions. These effects will be difficult to reproduce with average atom models that describe mixtures of dense atoms as a collection of noninteracting species.

With the nuclear configurations extracted from the MD trajectories, we can determine the local structure of the plasma as a function of the density and temperature. In Fig. 6, we illustrate changes in these structures with a series of pair correlation functions. With increasing density and decreasing temperature, the liquid becomes more structured, and the peaks in the correlation functions increase. Under no conditions we found a signature of a stable molecular bond between Mg and O species. However, the Mg and O nuclei exhibit positive correlations that are slightly stronger than those between the other pairs. This was seen in Ref. 82 and is due to an imbalance in their respective charge states. In comparison to our recent work[33] on boron nitride (BN) which shows a structure-less feature in $g(r)$ at 5×10^4–10^5 K, our results on MgO show that

correlation remains up to 5×10^5 K. This is consistent with the electronic structure analysis above and indicates that an average-atom approach would be less trustworthy for MgO at below 5×10^5 K, higher than that for BN (10^5 K) because of the deeper K shells of Mg and O than B and N.

C. Single and multishock Hugoniot curves

Dynamic shock compression experiments allow one to directly measure the equation of state and other physical properties of hot, dense fluids. Such experiments are often used to determine the principal Hugoniot curve, which is the locus of final states that can be obtained from different shock velocities. Density functional theory has been validated by experiments as an accurate tool for predicting the shock compression of a variety of different materials.[44-46]

During a shock wave experiment, a material whose initial state is characterized by an internal energy, pressure, and volume (E_0, P_0, V_0) will change to a final state denoted by (E, P, V) while conserving the mass, momentum, and energy. This leads to the Rankine-Hugoniot relation,[83]

$$(E - E_0) + \frac{1}{2}(P + P_0)(V - V_0) = 0. \qquad (6)$$

Here, we solve this equation for our computed first-principles EOS data set, only in the liquid phase. We obtain a continuous Hugoniot curve by interpolating the EOS data with splines as a function of ρ and T. The Hugoniot curve for the liquid state only depends on the liquid EOS and the initial point but not on the path followed in the solid phases. In order to obtain the principal Hugoniot curve, we used initial conditions based on the energy and pressure
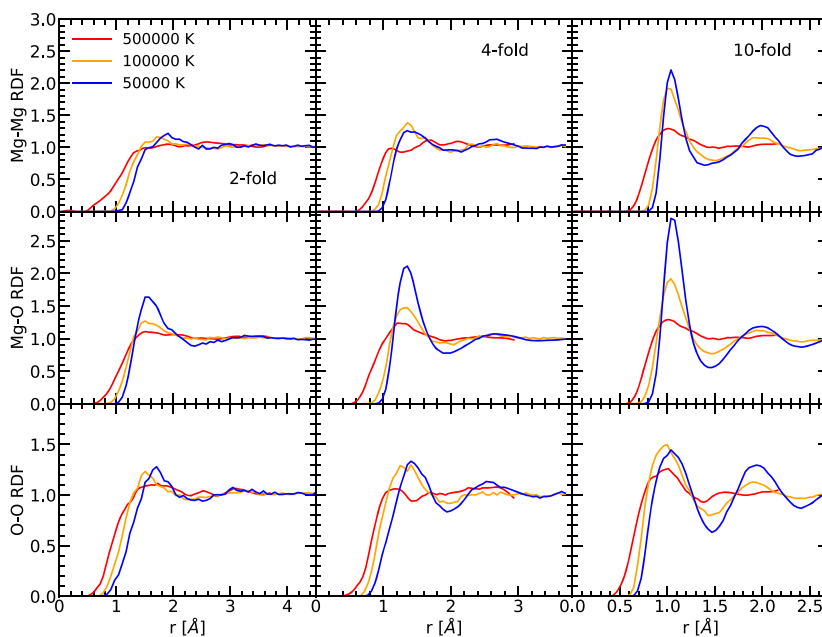

FIG. 6. Nuclear pair correlation functions 2-fold (left), 4-fold (middle), and 10-fold compression (right column) at different temperatures given in the legend. The different rows show these functions for Mg–Mg, Mg–O, and O–O pairs of nuclei.

of ambient, solid MgO in the B1 phase computed with static DFT calculations at the experimental density of 3.570 g cm^{-3} (V_0 = 18.747 8216 Å^3/MgO). Depending on which DFT functional we use, we obtained two slightly different initial energies, E_0^{LDA} = −274.613 8119 and E_0^{PBE} = −275.337 0951 hartree/MgO. The difference between these two values is small compared the ~50 000 hartree/MgO that the internal energy changes along the shock Hugoniot curve in the temperature interval that we study here. However, one would want to make reasonable choice to minimize the error that arises from choosing a particular DFT functional. Thus, when we evaluate the $(E − E_0)$ term in Eq. (6), we use values derived with the same functional. When we use PIMC values for E, we combine them with E_0^{PBE} because this has worked well in Ref. 37. The resulting shock Hugoniot curve has been added to Figs. 1, 3, and 7–9.

The principal Hugoniot curve in Figs. 7 and 8 exhibits a wide pressure interval where the compression ratio exceeds 4.0, the asymptotic value for a nonrelativistic ideal gas. Such high compression values are the result of excitations of internal degrees of freedom,[29] which increase the internal energy term in Eq. (6). Consequently, the second term in this equation becomes more negative, which reduces the volume V and thus increases the compression ratio. Indeed, at a pressure of 18 666 GPa and a temperature of 525 000 K, the shock compression ratio starts to exceed 4, which are conditions where the L shell electrons are already ionized. The bulk of the high compression region is dominated by the ionization of the K shell (1s) electrons of the Mg and O nuclei. However, instead of two separate compression peaks, we see a broad region of increased compression indicating that the two peaks have merged due to interaction effects.[39] No experimental data are available in the K- and L-shell ionization regimes yet. In the TPa regime, we obtain an excellent agreement between our predictions and the experimental data by Root et al.[23] and McCoy et al.[24] (see Fig. 8), which underlines the robustness of our DFT-MD calculations.

FIG. 8. The MgO shock Hugoniot curve in the pressure-compression plane. The symbols show the experimental results by Root et al.[23] and by McCoy et al.[24] The inset enlarges the lower pressure region.

The highest compression ratio of 4.66 is reached for 6.73 × 10^7 K and 421 000 GPa, which coincides in pressure with the upper compression maximum of the shock Hugoniot curve of pure silicon, which has also been attributed to K shell ionization.[36] Based on this comparison and the K shell ionization analysis of MgO in Fig. 4, we conclude that the upper part of the high compression region in Fig. 7 is dominated by the ionization of the K shell electrons of the Mg nuclei, while the lower end around 10^5 GPa and 2 × 10^6 K marks the beginning of the K shell ionization of the oxygen ions, as shown in Fig. 4. However, in shock compressed pure oxygen, the K shell ionization peak occurs for lower P and T. We attribute this difference to the interaction effects in hot, dense MgO that can shift the compression peaks along the Hugoniot curve to higher temperatures and pressures and reduce the peak compression.[39]

It is interesting to note that we do not see a separate compression maximum for the L shell ionization, while such maxima were
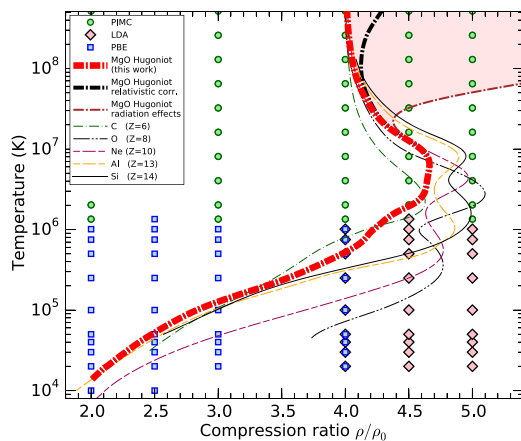

FIG. 7. The MgO shock Hugoniot curve with and without relativistic and radiation effects are compared with the Hugoniot curves of carbon,[30,70] oxygen,[72] neon,[31] aluminum,[38] and silicon.[32,36] This comparison supports the interpretation that the broad temperature interval where the compression of MgO exceeds 4.5 can be attributed to the ionization of the K shell electrons of the oxygen and magnesium nuclei.
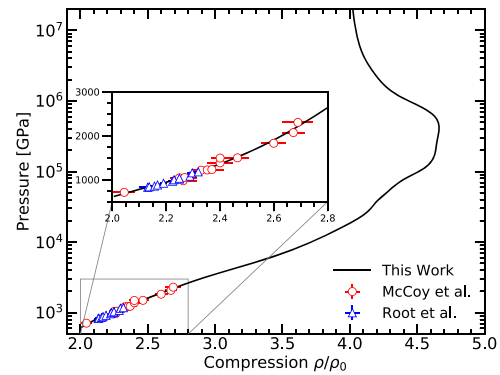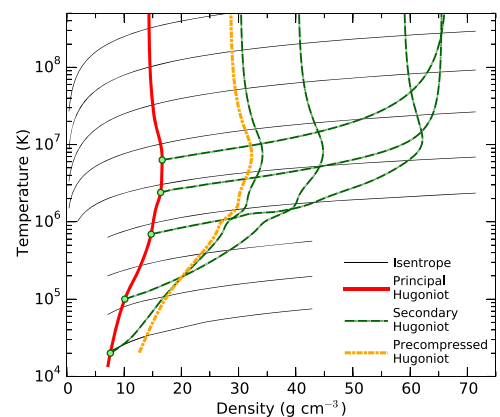

FIG. 9. Single and double shock Hugoniot curves are compared with a family of isentropes. For weak second shocks, minimal shock heating is introduced and the secondary Hugoniot curves behave like isentropes. For stronger second shocks, the heating is substantial and the resulting Hugoniot curve is similar to the shock curve for a precompressed sample.

seen in simulations of pure nitrogen and oxygen.[38,64] In Figs. 7 and 8, we instead see a slight lowering in temperature, or pressure, respectively, from approximately 3.2 to 4.2-fold compression, which we attribute to the L-shell ionization of the Mg and O nuclei because the same shape was seen in simulations of dense CH plastic and associated with the ionization of the L-shell of the carbon nuclei (see Fig. 3 of Ref. 66). We conclude that L shells of the Mg and O nuclei are ionized gradually, as it occurs in dense carbon and boron materials.[33,40,47] This interpretation is consistent with the electronic structure observed in Fig. 5 where the oxygen and magnesium electronic states are strongly hybridized at high compression.

The Hugoniot curves in Figs. 7 and 8 show a small shoulder at 4.3-fold compression. We determined this to be a robust feature even though we switch between DFT-MD and PIMC data sets in this regime. Our EOS table (see the supplementary material) is sufficiently dense so that different interpolation schemes for the pressure and internal energy yield consistent results. For example, even with linear interpolation, we have obtained very similar Hugoniot curves.

Very approximately, we added relativistic and radiation effects to the Hugoniot curves in Fig. 7. Under the assumption of complete ionization, the relativistic corrections were derived for an ideal gas of electrons. This increases the shock compression ratio for $P > 7 \times 10^6$ GPa and $T > 10^8$ K.

Considering an ideal black body scenario, we derived the photon contribution to the EOS using $P_{radiation} = (4\sigma/3c)T^4$ and $E_{radiation} = 3P_{radiation}V$, where σ is the Stefan-Boltzman constant and c is the speed of light in vacuum. We find that radiation effects are important only for temperatures above 2×10^7 K, which is above the temperature necessary to completely ionize the 1s orbitals of Mg and O species.

In Fig. 9, we show a number of double-shock Hugoniot curves. Various points along the principal Hugoniot curve were chosen as initial conditions for a second shock that compresses the material again reaching densities that are much higher than can be probed with single shocks. If one starts from the high compression point on the principal Hugoniot curve, one can reach densities of 65 g cm^{-3}. However, the compression ratio is typically not as high because the strength of the interaction effects increases and this lowers the compression ratio. For the secondary shock Hugoniot curves that we show in Fig. 9, the maximum compression ratio varied between 4.51 and 3.97, while the maximum compression ratio of the principal Hugoniot curve was 4.66.

Figure 9 also compares our secondary Hugoniot curves with our isentropes and isotherms. For weak second shocks, the secondary Hugoniot curves and isentropes almost coincide, which implies that the second shock produces very little irreversible heat. As the strength of the second shock increases, more and more irreversible heat is generated.

In Fig. 10, we compare an isentrope with various multishock Hugoniot curves in order to determine how closely one can trace an isentrope by breaking up a single shock into multiple smaller shocks. All curves start from 20 000 K, twice the ambient density, and 1386 GPa. The isentrope[84] was derived from our EOS table using $\frac{dT}{dV}|_S = -T\frac{dP}{dT}|_V / \frac{dE}{dT}|_V$. For weak shocks, the Hugoniot curve does not deviate much from an isentrope. For strong shocks, a substantial amount of shock heating occurs. The resulting single-shock Hugoniot curves are thus much hotter than an isentrope when
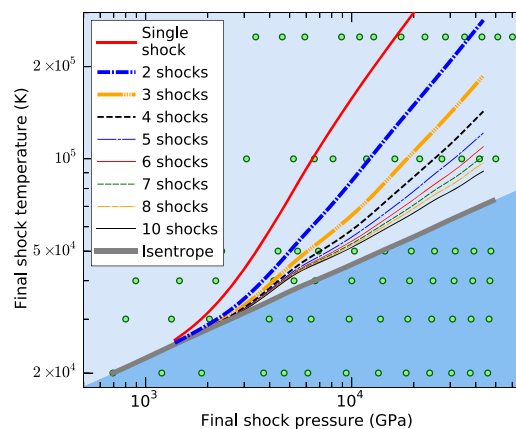

FIG. 10. The amount of shock heating can be reduced if multiple shocks are used to compress a material rather than just one. Here, we plot the final shock temperature as function of the final shock pressure for different numbers of shocks. The more shocks are employed, the closer the results are to an isentrope (thick gray line). 20 000 K and $\rho = 2\rho_0$ were chosen as initial conditions. The circles represent the DFT-MD simulation points that we used in this analysis.

both are compared for the same pressure. The discrepancy depends significantly on pressure, which reflects the fact that the final shock density cannot exceed 4.7-fold the initial density (Fig. 7). To reach a large final shock pressure, a substantial pressure contribution must come from the thermal pressure, which requires high temperatures.

One can, however, get arbitrarily close to isentropic compression by breaking up single shock experiments into multiple weaker shocks. The purpose of Fig. 10 is to assess quantitatively how well this method works for shocks in MgO and to determine how much shock heating still occurs if the shock is broken up into $N = 2-10$ steps. In our multishock calculations, we successively solve Eq. (6) to connect the intermediate shock states. In order to obtain the lowest possible shock temperature for a given number of shocks, we keep the final shock pressure fixed, while we carefully adjust the temperatures of the intermediate shocks until we determined the global minimum of the final shock temperature with sufficient accuracy.

As expected, all the resulting multishock Hugoniot curves converge to an isentrope for weak shocks. For strong shocks such as $P_{final}/P_{initial} \approx 31$, we find that the temperature of single-shock is 8.36 times higher than the corresponding temperature on the isentrope. If this shock is broken up into two, well-chosen smaller shocks, the final shock temperature be reduced to 4.00 times the value on the isentrope. If three, four, five, or even 10 shocks are employed, the final shock temperature can, respectively, be reduced to 2.64, 2.02, 1.72, or 1.29 times the isentropic value. These are substantial reductions compared to the single-shock temperatures.

IV. CONCLUSION

By combining results from PIMC and DFT-MD simulations, we provided a consistent EOS table for MgO in the regime of warm,

dense matter (see the supplementary material), which includes conditions where the K- and L-shell electrons of both nuclei are ionized. The ionization of the L-shell only introduces a small increase in compression along the shock Hugoniot curve. The K shell ionization of both nuclei, however, introduces a broad temperature interval where shock compression exceeds values of 4.5. The maximum compression ratio of 4.66 is reached for conditions of 6 378 000 K and 420 900 GPa where the K-shell ionization of the Mg nuclei dominates. By analyzing the electronic density of states in simulations at lower temperatures, we demonstrate that the L-shells of Mg and O are strongly hybridized.

From the present work, it is clear that mixing magnesium and oxygen under extreme conditions has nonideal effects on the electronic structure and thus the ionization processes. This will make it challenging for other theoretical methods to approximate the properties of MgO by combining EOS tables of Mg and O without fully taking into account their interaction effects. However, this also demonstrates that elements with a relatively close atomic number may be strongly influenced by one another. This could have some significance for ICF experiments and for stellar interior opacities where the radiative properties and thus the ionization stage are of essence.

SUPPLEMENTARY MATERIAL

See the supplementary material for our equation of state provided as a table in text format. The columns contain the following quantities: (1) Simulation method: PIMC, DFT-MD with GGA (PBE), or LDA functional. (3) Volume per MgO formula unit in angstrom^3. (5) Mass density in g cm^{-3}. (7) Temperature in Kelvin. (9) Pressure in GPa. (10) 1-σ uncertainty of pressure. (12) Internal energy in hartree per MgO formula unit. The zero of energy is a fully ionized system without any kinetic energy. (13) 1-σ uncertainty of energy.

REFERENCES

[1] See http://exoplanet.eu/ for the Extrasolar Planets Encyclopedia.

[2] B. A. Hammel, S. W. Haan, D. S. Clark, M. J. Edwards, S. H. Langer, M. M. Marinak, M. V. Patel, J. D. Salmonson, and H. A. Scott, "High-mode Rayleigh-Taylor growth in NIF ignition capsules," High Energy Density Phys. **6**(2), 171–178 (2010) [2nd International Conference on High Energy Density Physics, ICHED 2009].

[3] D. E. Fratanduono, M. Millot, R. G. Kraus, D. K. Spaulding, G. W. Collins, P. M. Celliers, and J. H. Eggert, "Thermodynamic properties of MgSiO$_3$ at super-Earth mantle conditions," Phys. Rev. B **97**(21), 214105 (2018).

[4] D. Valencia, M. Ikoma, T. Guillot, and N. Nettelmann, "Composition and fate of short-period super-Earths," Astron. Astrophys. **516**, A20 (2010).

[5] R. M. Bolis, G. Morard, T. Vinci, A. Ravasio, E. Bambrink, M. Guarguaglini, M. Koenig, R. Musella, F. Remus, J. Bouchet, N. Ozaki, K. Miyanishi, T. Sekine, Y. Sakawa, T. Sano, R. Kodama, F. Guyot, and A. Benuzzi-Mounaix, "Decaying shock studies of phase transitions in MgO-SiO$_2$ systems: Implications for the super-Earths' interiors," Geophys. Res. Lett. **43**(18), 9475–9483, https://doi.org/doi:10.1002/2016gl070466 (2016).

[6] S. Seager, M. Kuchner, C. A. Hier-Majumder, and B. Militzer, "Mass-radius relationships for solid exoplanets," Astrophys. J. **669**(2), 1279–1297 (2007).

[7] D. Valencia, R. J. O'Connell, and D. D. Sasselov, "The role of high-pressure experiments on determining super-Earth properties," Astrophys. Space Sci. **322**(1-4), 135–139 (2009).

[8] F. W. Wagner, N. Tosi, F. Sohl, H. Rauer, and T. Spohn, "Rocky super-Earth interiors," Astron. Astrophys. **541**, A103 (2012).

[9] D. G. Hicks, T. R. Boehly, J. H. Eggert, J. E. Miller, P. M. Celliers, and G. W. Collins, "Dissociation of liquid silica at high pressures and temperatures," Phys. Rev. Lett. **97**(2), 025502 (2006).

[10] M. Millot, N. Dubrovinskaia, A. Černok, S. Blaha, L. Dubrovinsky, D. G. Braun, P. M. Celliers, G. W. Collins, J. H. Eggert, and R. Jeanloz, "Shock compression of stishovite and melting of silica at planetary interior conditions," Science **347**(6220), 418–420 (2015).

[11] R. S. McWilliams, D. K. Spaulding, J. H. Eggert, P. M. Celliers, D. G. Hicks, R. F. Smith, G. W. Collins, and R. Jeanloz, "Phase transformations and metallization of magnesium oxide at high pressure and temperature," Science **338**(6112), 1330–1333 (2012).

[12] K. Miyanishi, Y. Tange, N. Ozaki, T. Kimura, T. Sano, Y. Sakawa, T. Tsuchiya, and R. Kodama, "Laser-shock compression of magnesium oxide in the warm-dense-matter regime," Phys. Rev. E **92**(2), 023103 (2015).

[13] F. Soubiran and B. Militzer, "Electrical conductivity and magnetic dynamos in magma oceans of super-Earths," Nat. Commun. **9**(1), 3883 (2018).

[14] T. S. Duffy, R. J. Hemley, and H.-k. Mao, "Equation of state and shear strength at multimegabar pressures: Magnesium oxide to 227 GPa," Phys. Rev. Lett. **74**(8), 1371 (1995).

[15] A. B. Belonoshko and L. S. Dubrovinsky, "Molecular dynamics of NaCl (B1 and B2) and MgO (B1) melting: Two-phase simulation," Am. Mineral. **81**(3-4), 303–316 (1996).

[16] B. Boates and S. A. Bonev, "Demixing instability in dense molten MgSiO$_3$ and the phase diagram of MgO," Phys. Rev. Lett. **110**(13), 135504 (2013).

[17] J. Bouchet, F. Bottin, V. Recoules, F. Remus, G. Morard, R. M. Bolis, and A. Benuzzi-Mounaix, "*Ab initio* calculations of the B1-B2 phase transition in MgO," Phys. Rev. B **99**(9), 094113 (2019).

[18] H. F. Wilson and B. Militzer, "Rocky core solubility in Jupiter and giant exoplanets," Phys. Rev. Lett. **108**(11), 111101 (2012).

[19] T. Tsuchiya, J. Tsuchiya, K. Umemoto, and R. M. Wentzcovitch, "Phase transition in MgSiO$_3$ perovskite in the earth's lower mantle," Earth Planet. Sci. Lett. **224**(3-4), 241–248 (2004).

[20] K. Umemoto and R. M. Wentzcovitch, "Two-stage dissociation in MgSiO$_3$ post-perovskite," Earth Planet. Sci. Lett. **311**(3-4), 225–229 (2011).

[21] K. Umemoto, R. M. Wentzcovitch, S. Wu, M. Ji, C.-z. Wang, and K.-m. Ho, "Phase transitions in MgSiO$_3$ post-perovskite in super-Earth mantles," Earth Planet. Sci. Lett. **478**, 40 (2017).

[22] O. V. Fat'yanov, P. D. Asimow, and T. J. Ahrens, "Thermodynamically complete equation of state of MgO from true radiative shock temperature measurements on samples preheated to 1850 K," Phys. Rev. B **97**, 024106 (2018).

[23] S. Root, L. Shulenburger, R. W. Lemke, D. H. Dolan, T. R. Mattsson, and M. P. Desjarlais, "Shock response and phase transitions of MgO at planetary impact conditions," Phys. Rev. Lett. **115**, 198501 (2015).

[24] C. A. McCoy, M. C. Marshall, D. N. Polsin, D. E. Fratanduono, P. M. Celliers, D. D. Meyerhofer, and T. R. Boehly, "Hugoniot, sound velocity, and shock temperature of MgO to 2300 GPa," Phys. Rev. B **100**, 014106 (2019).

[25] T. Taniuchi and T. Tsuchiya, "The melting points of MgO up to 4 TPa predicted based on the *ab initio* thermodynamic integration molecular dynamics," J. Phys.: Condens. Matter **30**(11), 114003 (2018).

[26] D. Alfè, "Melting curve of MgO from first-principles simulations," Phys. Rev. Lett. **94**(23), 235701 (2005).

[27] N. de Koker and L. Stixrude, "Self-consistent thermodynamic description of silicate liquids, with application to shock melting of MgO periclase and $MgSiO_3$ perovskite," Geophys. J. Int. **178**(1), 162–179 (2009).

[28] F. González-Cataldo, F. Soubiran, H. Peterson, and B. Militzer, "Path integral Monte Carlo and density functional molecular dynamics simulations of warm, dense $MgSiO_3$," Phys. Rev. B (submitted).

[29] B. Militzer, "First principles calculations of shock compressed fluid helium," Phys. Rev. Lett. **97**, 175501 (2006).

[30] L. X. Benedict, K. P. Driver, S. Hamel, B. Militzer, T. Qi, A. A. Correa, A. Saul, and E. Schwegler, "A multiphase equation of state for carbon addressing high pressures and temperatures," Phys. Rev. B **89**, 224109 (2014).

[31] K. P. Driver and B. Militzer, "First-principles simulations and shock Hugoniot calculations of warm dense neon," Phys. Rev. B **91**(4), 045103 (2015).

[32] S. X. Hu, B. Militzer, L. A. Collins, K. P. Driver, and J. D. Kress, "First-principles prediction of the softening of the silicon shock Hugoniot curve," Phys. Rev. B **94**, 094109 (2016).

[33] S. Zhang, A. Lazicki, B. Militzer, L. H. Yang, K. Caspersen, J. A. Gaffney, M. W. Däne, J. E. Pask, W. R. Johnson, A. Sharma, P. Suryanarayana, D. D. Johnson, A. V. Smirnov, P. A. Sterne, D. Erskine, R. A. London, F. Coppari, D. Swift, J. Nilsen, A. J. Nelson, and H. D. Whitley, "Equation of state of boron nitride combining computation, modeling, and experiment," Phys. Rev. B **99**, 165103 (2019).

[34] D. M. Ceperley, "Path integrals in the theory of condensed helium," Rev. Mod. Phys. **67**, 279–355 (1995).

[35] D. Ceperley, *Monte Carlo and Molecular Dynamics of Condensed Matter Systems* (Editrice Compositori, Bologna, Italy, 1996), Vol. 49, p. 443.

[36] B. Militzer and K. P. Driver, "Development of path integral Monte Carlo simulations with localized nodal surfaces for second-row elements," Phys. Rev. Lett. **115**(17), 176403 (2015).

[37] S. Zhang, K. P. Driver, F. Soubiran, and B. Militzer, "Equation of state and shock compression of warm dense sodium—A first-principles study," J. Chem. Phys. **146**(7), 074505 (2017).

[38] K. P. Driver, F. Soubiran, and B. Militzer, "Path integral Monte Carlo simulations of warm dense aluminum," Phys. Rev. E **97**(6), 063207 (2018).

[39] B. Militzer, "Path integral Monte Carlo and density functional molecular dynamics simulations of hot, dense helium," Phys. Rev. B **79**, 155105 (2009).

[40] S. Zhang, B. Militzer, L. X. Benedict, F. Soubiran, P. A. Sterne, and K. P. Driver, "Path integral Monte Carlo simulations of dense carbon-hydrogen plasmas," J. Chem. Phys. **148**(10), 102318 (2018).

[41] P. Hohenberg and W. Kohn, "Inhomogeneous electron gas," Phys. Rev. **136**, B864–B871 (1964).

[42] W. Kohn and L. J. Sham, "Self-consistent equations including exchange and correlation effects," Phys. Rev. **140**, A1133–A1138 (1965).

[43] N. David Mermin, "Thermal properties of the inhomogeneous electron gas," Phys. Rev. **137**, A1441–A1443 (1965).

[44] S. Root, R. J. Magyar, J. H. Carpenter, D. L. Hanson, and T. R. Mattsson, "Shock compression of a fifth period element: Liquid xenon to 840 GPa," Phys. Rev. Lett. **105**, 085501 (2010).

[45] X. Wang, F. Tian, L. Wang, T. Cui, B. Liu, and G. Zou, "Structural stability of polymeric nitrogen: A first-principles investigation," J. Chem. Phys. **132**(2), 024502 (2010).

[46] T. R. Mattsson, S. Root, A. E. Mattsson, L. Shulenburger, R. J. Magyar, and D. G. Flicker, "Validating density-functional theory simulations at high energy-density conditions with liquid krypton shock experiments to 850 GPa on Sandia's Z machine," Phys. Rev. B **90**, 184105 (2014).

[47] S. Zhang, B. Militzer, M. C. Gregor, K. Caspersen, L. H. Yang, J. Gaffney, T. Ogitsu, D. Swift, L. Amy, D. Erskine, R. A. London, P. M. Celliers, J. Nilsen, P. A. Sterne, and H. D. Whitley, "Theoretical and experimental investigation of the equation of state of boron plasmas," Phys. Rev. E **98**(2), 023205 (2018).

[48] V. V. Karasiev, L. Calderín, and S. B. Trickey, "Importance of finite-temperature exchange correlation for warm dense matter calculations," Phys. Rev. E **93**, 063207 (2016).

[49] E. L. Pollock and D. M. Ceperley, "Simulation of quantum many-body systems by path-integral methods," Phys. Rev. B **30**, 2555–2568 (1984).

[50] D. M. Ceperley, "Fermion nodes," J. Stat. Phys. **63**(5-6), 1237–1267 (1991).

[51] D. M. Ceperley, "Path-integral calculations of normal liquid ^3He," Phys. Rev. Lett. **69**, 331–334 (1992).

[52] C. Pierleoni, D. M. Ceperley, B. Bernu, and W. R. Magro, "Equation of state of the hydrogen plasma by path integral Monte Carlo simulation," Phys. Rev. Lett. **73**, 2145–2149 (1994).

[53] W. R. Magro, D. M. Ceperley, C. Pierleoni, and B. Bernu, "Molecular dissociation in hot, dense hydrogen," Phys. Rev. Lett. **76**, 1240–1243 (1996).

[54] B. Militzer, W. Magro, and D. Ceperley, "Characterization of the state of hydrogen at high temperature and density," Contrib. Plasma Phys. **39**(1-2), 151–154 (1999).

[55] B. Militzer, "Path integral Monte Carlo simulations of hot dense hydrogen," Ph.D. thesis, University of Illinois at Urbana-Champaign, 2000.

[56] B. Militzer and D. M. Ceperley, "Path integral Monte Carlo calculation of the deuterium Hugoniot," Phys. Rev. Lett. **85**(9), 1890–1893 (2000).

[57] B. Militzer and D. M. Ceperley, "Path integral Monte Carlo simulation of the low-density hydrogen plasma," Phys. Rev. E **63**, 066404 (2001).

[58] B. Militzer, D. M. Ceperley, J. D. Kress, J. D. Johnson, L. A. Collins, and S. Mazevet, "Calculation of a deuterium double shock Hugoniot from *ab initio* simulations," Phys. Rev. Lett. **87**, 275502 (2001).

[59] B. Militzer, "Correlations in hot dense helium," J. Phys. A: Math. Theor. **42**(21), 214001 (2009).

[60] B. Militzer, "Hydrogen–helium mixtures at high pressure," J. Low Temp. Phys. **139**(5), 739–752 (2005).

[61] M. D. Jones and D. M. Ceperley, "Crystallization of the one-component plasma at finite temperature," Phys. Rev. Lett. **76**, 4572–4575 (1996).

[62] E. L. Pollock and B. Militzer, "Dense plasma effects on nuclear reaction rates," Phys. Rev. Lett. **92**, 021101 (2004).

[63] B. Militzer and E. L. Pollock, "Equilibrium contact probabilities in dense plasmas," Phys. Rev. B **71**, 134303 (2005).

[64] K. P. Driver and B. Militzer, "First-principles equation of state calculations of warm dense nitrogen," Phys. Rev. B **93**, 064101 (2016).

[65] K. P. Driver and B. Militzer, "First-principles simulations of warm dense lithium fluoride," Phys. Rev. E **95**(4), 043205 (2017).

[66] S. Zhang, K. P. Driver, F. Soubiran, and B. Militzer, "First-principles equation of state and shock compression predictions of warm dense hydrocarbons," Phys. Rev. E **96**(1), 013204 (2017).

[67] V. Natoli and D. M. Ceperley, "An optimized method for treating long-range potentials," J. Comput. Phys. **117**(1), 171–178 (1995).

[68] B. Militzer, "Computation of the high temperature Coulomb density matrix in periodic boundary conditions," Comput. Phys. Commun. **204**, 88 (2016).

[69] B. Militzer, E. L. Pollock, and D. M. Ceperley, "Path integral Monte Carlo calculation of the momentum distribution of the homogeneous electron gas at finite temperature," High Energy Density Phys. **30**, 13–20 (2019).

[70] K. P. Driver and B. Militzer, "All-electron path integral Monte Carlo simulations of warm dense matter: Application to water and carbon plasmas," Phys. Rev. Lett. **108**(11), 115502 (2012).

[71] G. Kresse and D. Joubert, "From ultrasoft pseudopotentials to the projector augmented-wave method," Phys. Rev. B **59**(3), 1758–1775 (1999).

[72] K. P. Driver, F. Soubiran, S. Zhang, and B. Militzer, "First-principles equation of state and electronic properties of warm dense oxygen," J. Chem. Phys. **143**, 164507 (2015).

[73] S. Nosé, "A unified formulation of the constant temperature molecular dynamics methods," J. Chem. Phys. **81**, 511–519 (1984).

[74] S. Nosé, "Constant temperature molecular dynamics methods," Prog. Theor. Phys. Suppl. **103**, 1 (1991).

[75] P. E. Blöchl, "Projector augmented-wave method," Phys. Rev. B **50**(24), 17953–17979 (1994).

[76] J. P. Perdew, K. Burke, and M. Ernzerhof, "Generalized gradient approximation made simple," Phys. Rev. Lett. **77**(18), 3865–3868 (1996).

[77] G. Chabrier and A. Y. Potekhin, "Equation of state of fully ionized electron-ion plasmas," Phys. Rev. E **58**, 4941 (1998).

[78] G. Chabrier, S. Mazevet, and F. Soubiran, Astrophys. J. **872**, 51 (2019).

[79] B. Militzer and W. B. Hubbard, "*Ab initio* equation of state for hydrogen-helium mixtures with recalibration of the giant-planet mass-radius relation," Astrophys. J. **774**, 148 (2013).

[80] General Atomic and Molecular Electronic Structure System (GAMESS), visit http://www.msg.ameslab.gov/gamess/ for more information.

[81] K. P. Driver, F. Soubiran, S. Zhang, and B. Militzer, "Comparison of path integral Monte Carlo simulations of helium, carbon, nitrogen, oxygen, water, neon, and silicon plasmas," High Energy Density Phys. **23**, 81–89 (2017).

[82] D. Cebulla and R. Redmer, "*Ab initio* simulations of MgO under extreme conditions," Phys. Rev. B **89**(13), 134107 (2014).

[83] Y. B. Zeldovich and Y. P. Raizer, *Elements of Gasdynamics and the Classical Theory of Shock Waves* (Academic Press, New York, 1968).

[84] B. Militzer and W. H. Hubbard, Astrophys. Space Sci. **322**, 129 (2009).

[85] S. D. Crockett and S. Rudin, "Lithium fluoride equations of state (SESAME 7271)," Technical Report No. LA-UR-06-8401, Los Alamos National Laboratory, 2006, available at http://permalink.lanl.gov/object/view?what=info:lanl-repo/lareport/LA-UR-06-8401.

[86] R. M. More, K. H. Warren, D. A. Young, and G. B. Zimmerman, "A new quotidian equation of state (QEOS) for hot dense matter," Phys. Fluids **31**, 3059–3078 (1988).